

PRECEDING PAGE BLANK NOT FILMED.

XXIII. Spacecraft Radio

TELECOMMUNICATIONS DIVISION

N67-29164

A. The Mariner S-Band Turnaround Ranging Transponder Improvement Program, L. M. Hershey

Some results of the study being made of the S-band turnaround ranging transponder used on *Mariner C* were described in SPS 37-42, Vol. IV, pp. 183-189, and SPS 37-43, Vol. IV, pp. 374-376. This study is conducted by the Space and Re-Entry Systems Division of the Philco-Ford Corporation, formerly a part of the Western Development Laboratory (WDL) Division. In the more recent SPS article, the measured effects of temperature and signal level variations on the turnaround ranging delay through the transponder are described for the whole transponder and for the individual groupings of modules termed "six-packs."

The next step in the study is measurement of the effect on overall transponder performance of environmental variations on each module individually. To date, only the 9.56-MHz IF amplifier module has been evaluated in this manner; its effect on ranging delay is shown in Fig. 1. The IF amplifier is not in the turnaround ranging loop, but is a part of the automatic phase control (APC) loop that furnishes the reference signal for the ranging phase

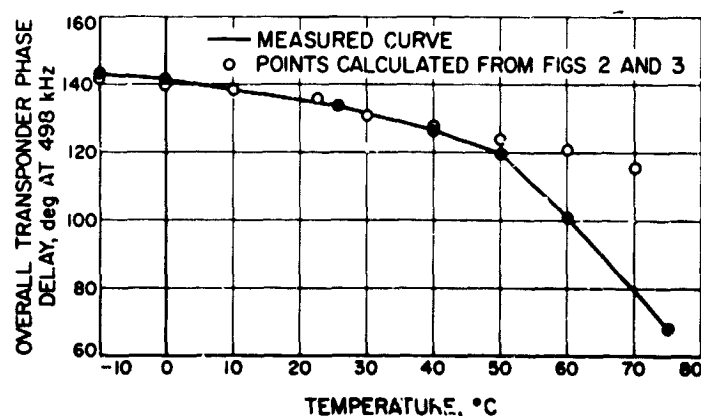


Fig. 1. Overall ranging delay variations from environmental variations on the 9.56 MHz IF amplifier

detector. It was hypothesized, therefore, that the change in the phase of the signal at the APC loop detector (caused by temperature variations), affected the ranging delay time at the ranging phase detector by changing the phase of the reference signal. To determine the validity of this hypothesis, a measurement was made of the effect of the ranging detector reference signal phase on the

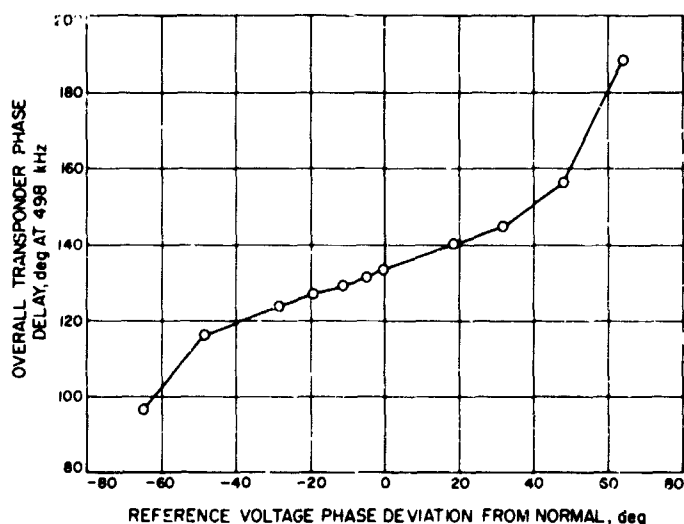


Fig. 2. Overall ranging delay vs ranging detector reference voltage phase

ranging delay through the transponder. The result, a strong effect, is shown in Fig. 2.

The hypothesis was further tested by a measurement of the RF phase shift through the IF amplifier as a function of temperature; this is shown in Fig. 3. The results of Figs. 2 and 3 were used to calculate the effect of temperature on ranging delay; the results were entered as points on Fig. 1. Agreement is shown between -10°C and 40°C , but the results deviate sharply at temperatures above this. It is tentatively concluded that the hypothesis is partially correct, but that some other mechanism is also contributing, and that the effect of the other mechanism is predominant at higher temperatures.

The effect of reference phase on the ranging delay cannot be explained by the analytical model usually used for a phase detector. Eventually, an effort should be made

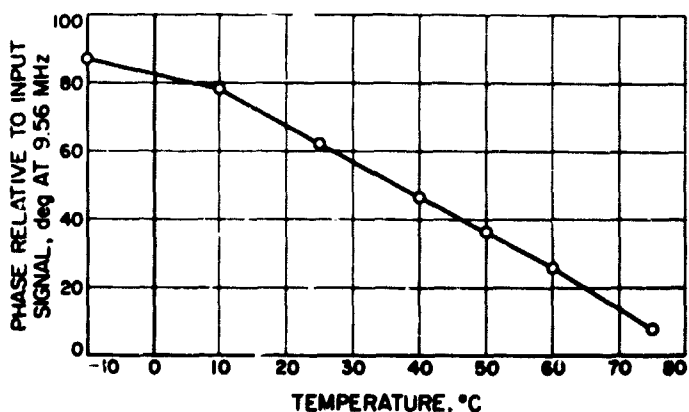


Fig. 3. IF amplifier phase variations vs temperature

to determine whether this is the result of a faulty analytical model, or deviations of the hardware from the expected performance. However, an investigation of the problem is not planned at this time.

It should be noted that the 9.56 MHz IF amplifier used in these tests exhibits phase shifts in excess of the limits specified for this module, although it had been previously tested (and passed) to these specifications. Referring to Fig. 3, the specified limit of ± 15 deg phase variation through the IF would result in a 10 deg overall ranging delay variation, which is a major contribution to the total.

The study continues with evaluation of the effect of the 9.56 MHz IF amplifier upon ranging delay, with the measurement of ranging delay where other individual modules are subjected to temperature variations, and with the measurement of doppler delay variations through the transponder at the S-band planned for the near future.

B. Spacecraft Guidance Radar Beam

Configuration Performance, R. L. Hottor

1. Introduction

This article concerns a part of the continuing effort to analyze the performance of the beam configuration of spacecraft guidance radars. These radars are used in closed loop guidance systems for lunar and planetary soft landing vehicles. Previous work concerning the radar beam-to-surface incidence angles was reported in SPS 37-43, Vol. IV, pp. 376-380. This article will show that the quality of the radar output data is affected by the geometry of the radar beam configuration, so much so that the performance of the beam configuration may be assessed by the quality of the radar output. Several radar functions make suitable criteria of quality. These are:

- (1) Altitude marking accuracy
- (2) Slant range estimation bias
- (3) Variances of the velocity and range estimates

For each of these criteria, beam geometry performance varies with changes in the beam look angle. The important criterion of estimation variance will be discussed in a future article.

The results in this article can be used to pick a beam geometry suitable for a given set of spacecraft trajectory and attitude conditions. The beam geometry chosen for

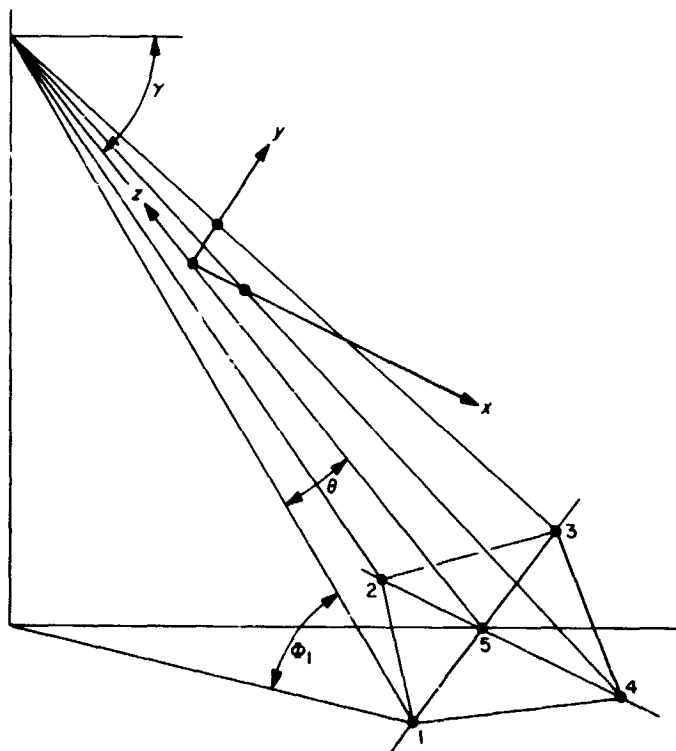


Fig. 4. Five-beam radar configuration

this work is particularly applicable to a Mars soft lander. Fig. 4 illustrates a simple five-beam configuration with four beams pointed symmetrically at an angle from the fifth. The radar measures range along beam 5, and the velocity vector in transverse and axial coordinates, as indicated in the figure. Information from each of the five beams may be combined in several ways to generate the required output information. Basically, the techniques discussed here use 3, 4, or 5 beams to perform the required function.

2. Altitude Marking Accuracy

All lunar or planetary soft landing concepts require some means to start the landing sequence. For this purpose, a range or altitude marking radar may be used to generate a signal when the surface distance in a given direction reaches a predetermined value. The signal is called a range mark. In an arbitrary radar beam configuration where true altitude may be desired to initiate the landing sequence, the beam most nearly vertical clearly gives the best approximation of true altitude. Altitude marking accuracy, therefore, is a function of vehicle attitude, trajectory incidence angle with respect to the surface, and beam configuration. How marking accuracy varies with beam configuration is the principal topic of this section.

a. Variation of marking accuracy with trajectory angles. Changes in the beam configuration chosen for this discussion (Fig. 4) involve only variations in the look angle θ . The other three important angles in the problem are the roll axis surface incidence angle γ , the beam system roll angle ϕ from the vertical plane, and the i th beam surface incidence angle Φ_{ii} .

Altitude marking accuracy is the ratio of the altitude to the range along the steepest beam. More simply, accuracy is the sine of the beam incidence angle. Letting accuracy be $h(\theta, \phi, \gamma)$,

$$h(\theta, \phi, \gamma) = \sin \gamma \cos \theta + \cos \phi \cos \gamma \sin \theta \quad (1)$$

Two values of the roll angle ϕ are important. Beam 1 is in the vertical plane when $\phi = 0$, and, at a given trajectory angle, maximum marking accuracy occurs for this position. Minimum accuracy occurs at $\phi = \pi/4$ when two adjacent beams intersect the surface with equal angles. For a given value of the beam pointing angle, accuracy varies with the roll axis incidence angle γ . Fig. 5 demonstrates this dependence with the two roll positions, and representative pointing angles from 30 to 60 deg. Curve 3 for $h(0, 0, \gamma)$ is included in Fig. 5 for comparison. As might be expected, beam geometries with wider look angles achieve maximum marking accuracy at lower trajectory angles.

b. Optimum configuration for best marking accuracy. At this point, the best attainable accuracy with geometry that can be continuously adjusted to the optimum value should be considered. As before, the accuracy is denoted by $h(\theta, \phi, \gamma)$

$$h(\gamma, \phi, \theta) = \sin \gamma \cos \theta + \cos \phi \cos \gamma \sin \theta \quad (2)$$

Differentiating $h(\gamma, \theta, \phi)$ with respect to θ , and setting the result equal to zero,

$$h'_{\theta}(\gamma, \phi, \theta) = -\sin \gamma \sin \theta + \cos \phi \cos \gamma \cos \theta = 0 \quad (3)$$

The value of θ satisfying Eq. (3) is θ_M .

$$\begin{aligned} \tan \theta_M &= \cos \phi \cot \gamma \\ \theta_M &= \tan^{-1}(\cos \phi \cot \gamma) \end{aligned} \quad (4)$$

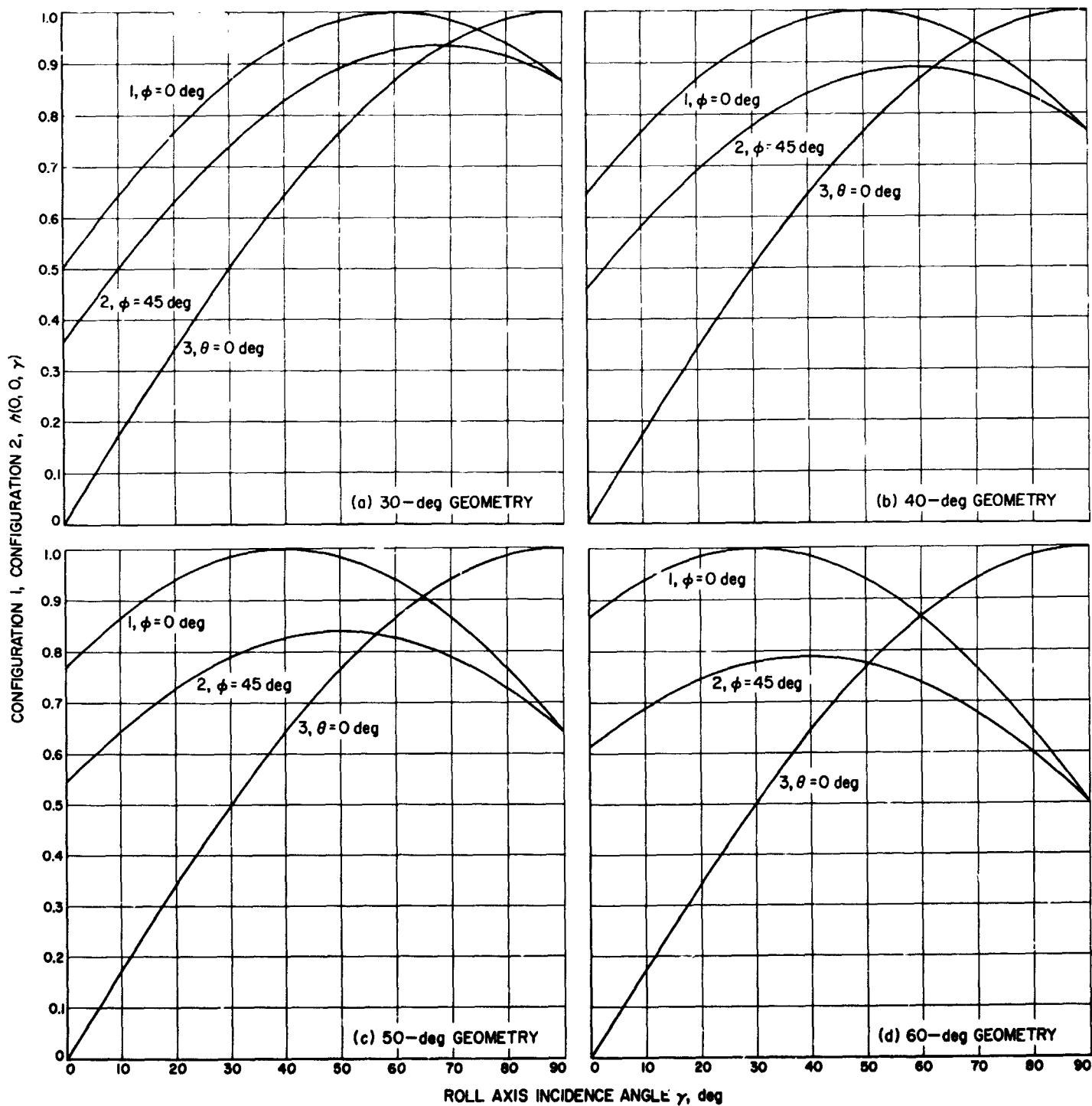


Fig. 5. Marking accuracy

Consequently, the following relations hold:

$$\cos \theta_M = \frac{1}{(1 + \cos^2 \phi \cot^2 \gamma)^{1/2}}$$

$$\sin \theta_M = \frac{\cos \phi \cot \gamma}{(1 + \cos^2 \phi \cot^2 \gamma)^{1/2}}$$

Substituting these values into Eq. (2),

$$h(\gamma, \phi, \theta_M) = \frac{\sin \gamma + \cos^2 \phi \cos \gamma \cot \gamma}{(1 + \cos^2 \phi \cot^2 \gamma)^{1/2}} \quad (5)$$

but this expression may be simplified. Multiplying numerator and denominator by $\sin \gamma$,

$$h(\gamma, \phi, \theta_M) = \frac{\sin^2 \gamma + \cos^2 \phi \cos^2 \gamma}{\sin \gamma (1 + \cos^2 \phi \cot^2 \gamma)^{1/2}}$$

$$= (\sin^2 \gamma + \cos^2 \phi \cos^2 \gamma)^{1/2} \quad (6)$$

This function is plotted in Fig. 6(a) for values of ϕ giving the extremes in roll position. Curve 3 for $h(0, 0, \gamma)$ is included again for comparison. The corresponding values of $h(\gamma, \phi, \theta_M)$ are

$$h(\gamma, 0, \theta_M) = 1.0 \quad (7)$$

$$h(\gamma, \pi/4, \theta_M) = \left(\sin^2 \gamma + \frac{\cos^2 \gamma}{2} \right)^{1/2}$$

$$= \frac{(1 + \sin^2 \gamma)^{1/2}}{(2)^{1/2}} \quad (8)$$

Values of θ_M as functions of γ are plotted in Fig. 6(b). When $\phi = 0$,

$$\theta_M = \tan^{-1}(\cot \gamma) \quad (9)$$

or

$$\theta_M = \frac{\pi}{2} - \gamma \quad (10)$$

When $\phi = \pi/4$,

$$\theta_M = \tan^{-1} \left(\frac{\cot \gamma}{(2)^{1/2}} \right) \quad (11)$$

Note that Fig. 6(a) and (b) have no bearing at all on Fig. 5(a) through (d), because maximum marking accu-

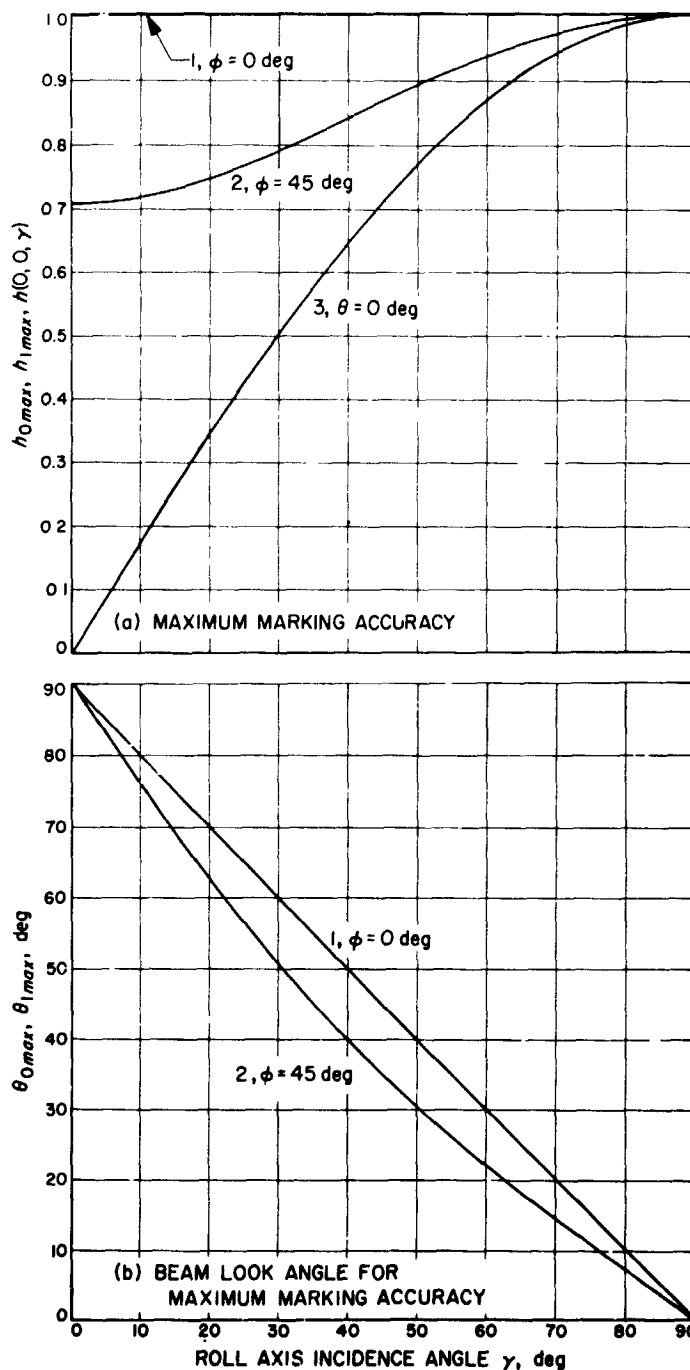


Fig. 6. Continuously adjusted beam look angle

racy is attained here by varying the geometry angle θ , whereas the maximum marking accuracy in paragraph a. occurred as the trajectory angle varied. It is not surprising, then, that these two maxima do not occur at the same trajectory angles.

3. Slant Range Bias Error

The guidance radar is also required to estimate range along the vehicle roll axis. This so-called slant range may

be measured directly along Beam 5, or by combining measurements of the other four beams. Slant range bias, as used here, refers to the error introduced by combining the range estimates of several beams. Specifically excluded are terrain bias errors that corrupt individual beam range estimates.

a. Analysis. For a three-beam configuration, slant range will be measured along the roll axis only, and, because it is measured directly, there will be no bias. For the four-beam configuration, however, range is derived from the average of the four outward pointing beams. The bias is accepted because the variance of the estimate takes

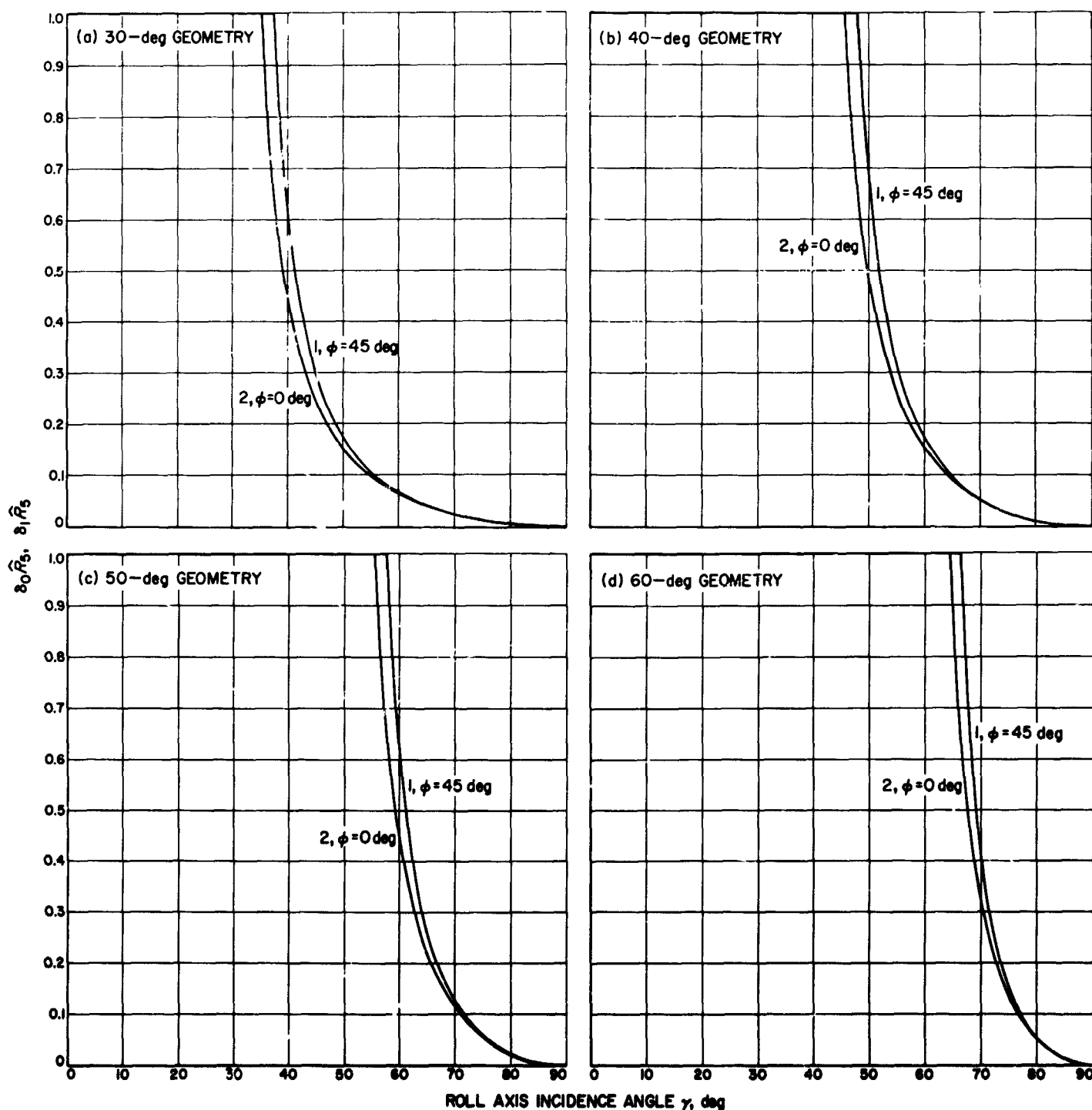


Fig. 7. Range bias for four beams

advantage of the noise averaging of four beams instead of one. A less noisy but biased range signal may be more desirable than an unbiased but noisy signal.

The range along each beam may be expressed in the terms of the vertical altitude and the sine of the beam incidence angle. Without loss of generality, unit altitude may be assumed. Eq. (12) shows an estimate of the range along the roll axis.

$$\begin{aligned}\hat{R}_s &= \frac{1}{4} (R_1 + R_2 + R_3 + R_4) \cos \theta \\ &= \frac{1}{4} \left(\frac{1}{\sin \Phi_{11}} + \frac{1}{\sin \Phi_{12}} + \frac{1}{\sin \Phi_{13}} + \frac{1}{\sin \Phi_{14}} \right) \cos \theta\end{aligned}\quad (12)$$

The bias is the difference between \hat{R}_s and the true value of R_s .

$$\begin{aligned}\hat{R}_s - R_s &= \frac{1}{4} \left(\frac{1}{\sin \Phi_{11}} + \frac{1}{\sin \Phi_{12}} + \frac{1}{\sin \Phi_{13}} + \frac{1}{\sin \Phi_{14}} \right) \\ &\quad \times \cos \theta - \frac{1}{\sin \gamma}\end{aligned}\quad (13)$$

The ratio of the bias to the true value is the percentage bias:

$$\begin{aligned}\frac{\hat{R}_s - R_s}{R_s} &= \frac{1}{4} \left(\frac{1}{\sin \Phi_{11}} + \frac{1}{\sin \Phi_{12}} + \frac{1}{\sin \Phi_{13}} + \frac{1}{\sin \Phi_{14}} \right) \\ &\quad \times \cos \theta \sin \gamma - 1.0\end{aligned}\quad (14)$$

$\sin \Phi_i$, however, may be expressed in the terms of the three angles γ , θ , and ϕ , which are defined in Fig. 4.

$$\sin \Phi_{1i} = \sin \gamma \cos \theta + \cos \left[\phi + (i-1) \frac{\pi}{2} \right] \cos \gamma \sin \theta \quad (15)$$

Substituting in Eq. (14) yields

$$\begin{aligned}\delta \hat{R}_s &= \frac{1}{4} \left(\frac{1}{\sin \gamma \cos \theta + \cos \phi \cos \gamma \sin \theta} \right. \\ &\quad + \frac{1}{\sin \gamma \cos \theta + \sin \phi \cos \gamma \sin \theta} \\ &\quad + \frac{1}{\sin \gamma \cos \theta - \cos \phi \cos \gamma \sin \theta} \\ &\quad \left. + \frac{1}{\sin \gamma \cos \theta - \sin \phi \cos \gamma \sin \theta} \right) \cos \theta \sin \gamma - 1.0\end{aligned}\quad (16)$$

Combining terms yields an expression more amenable to calculation:

$$\begin{aligned}\delta \hat{R}_s &= \frac{1}{4} \left(\frac{2 \sin^2 \gamma \cos^2 \theta}{\sin^2 \gamma \cos^2 \theta - \cos^2 \phi \cos^2 \gamma \sin^2 \theta} \right. \\ &\quad \left. + \frac{2 \sin^2 \gamma \cos^2 \theta}{\sin^2 \gamma \cos^2 \theta - \sin^2 \phi \cos^2 \gamma \sin^2 \theta} \right) - 1.0\end{aligned}\quad (17)$$

Dividing through by the numerator,

$$\begin{aligned}\delta \hat{R}_s &= \frac{1}{2} \left(\frac{1}{1 - \cos^2 \phi \cot^2 \gamma \tan^2 \theta} \right. \\ &\quad \left. + \frac{1}{1 - \sin^2 \phi \cot^2 \gamma \tan^2 \theta} \right) - 1.0\end{aligned}\quad (18)$$

Combining these terms gives

$$\delta \hat{R}_s = \frac{1}{2} \left(\frac{1 - \sin^2 \phi \cot^2 \gamma \tan^2 \theta + 1 - \cos^2 \phi \cot^2 \gamma \tan^2 \theta}{1 - \cot^2 \gamma \tan^2 \theta - \sin^2 \phi \cos^2 \phi \cot^4 \gamma \tan^4 \theta} \right) - 1.0 \quad (19)$$

Finally

$$\delta \hat{R}_s = \frac{1}{2} \left(\frac{2 - \cot^2 \gamma \tan^2 \theta}{1 - \cot^2 \gamma \tan^2 \theta - \sin^2 \phi \cos^2 \phi \cot^4 \gamma \tan^4 \theta} \right) - 1.0 \quad (20)$$

b. Discussion. Evaluation of this formidable expression presents few problems for a computer. The bias $\delta \hat{R}_s$ is plotted in Fig. 7 as a function of γ , the roll axis incidence angle, for some values of θ between 30 and 60 deg. Two

extremes in roll position are illustrated by two values of ϕ , namely, 0 and $\pi/4$. The bias curve for any other roll position of the beam geometry lies between the two curves drawn. Note that the bias approaches zero as the trajectory

approaches vertical. In this region, near touchdown, accuracy is most important.

C. Multipacting in Coaxial Transmission Lines at S-Band, R. Woo

1. Introduction

Experiments have been conducted to check for multipacting in $7/8$ -in. and $1\frac{5}{8}$ -in. rigid coaxial transmission lines in the frequency range of 1700 to 2400 MHz. The purpose of these experiments was twofold: (1) these frequencies and dimensions are typical RF spacecraft components, and data are needed; (2) the data can be checked against

previous data obtained at lower frequencies with a different test setup (SPS 37-41, Vol. IV, pp. 242-246) through scaling relations (SPS 37-36, Vol. IV, pp. 281-283).

2. Experimental apparatus

The experimental setup is shown in Fig. 8, and the schematic in Fig. 9. Approximately 1 kw CW of RF power was provided in the frequency range 1700 to 2400 MHz by a Philco 2000 klystron amplifier. A coaxial circulator with its isolated arm terminated in a $50\text{-}\Omega$ load was used to protect the klystron amplifier from large amounts of reflected power produced when breakdown occurs. Power level was varied by changing the drive level to the klystron amplifier. Both forward and reverse power levels

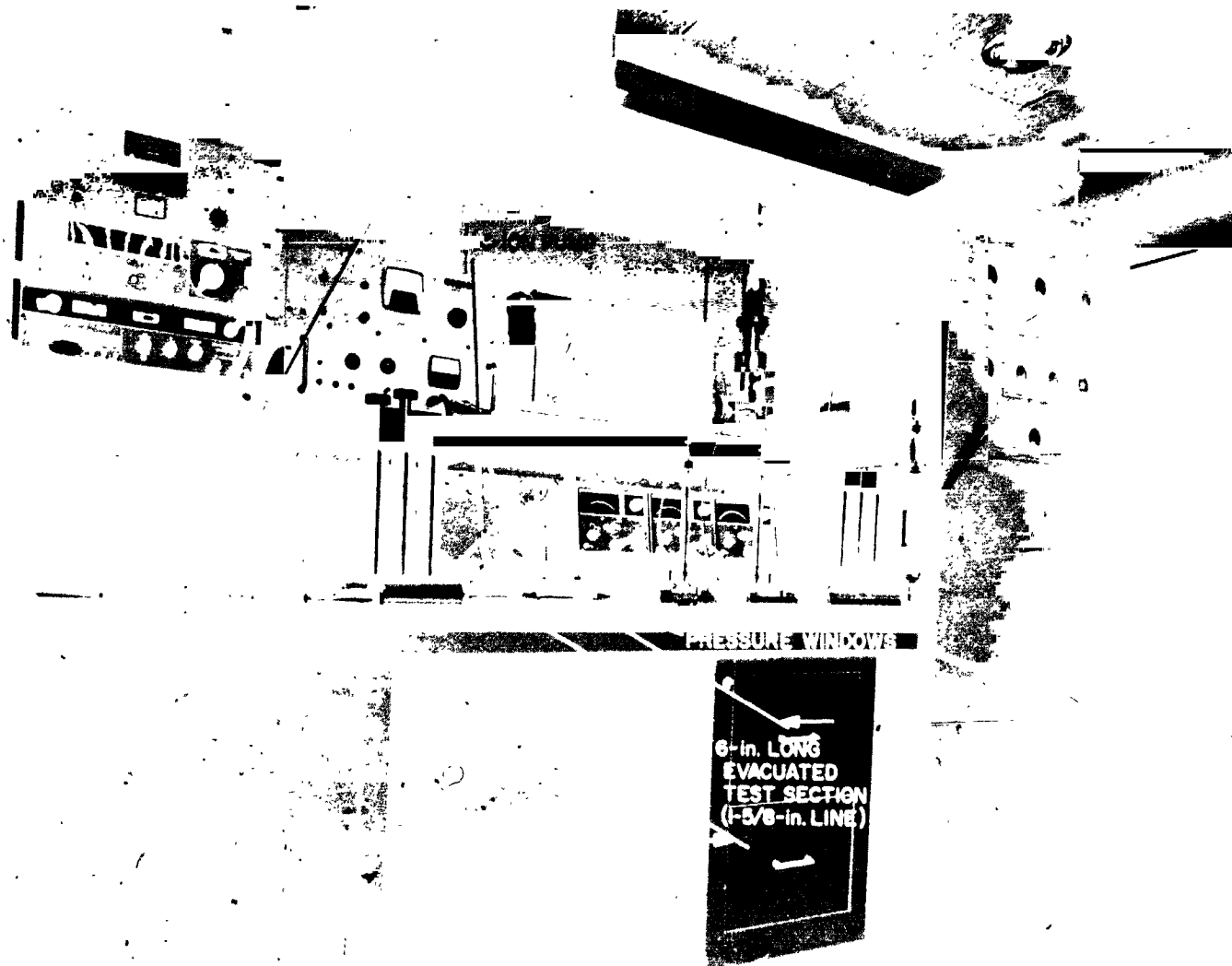


Fig. 8. Experimental setup

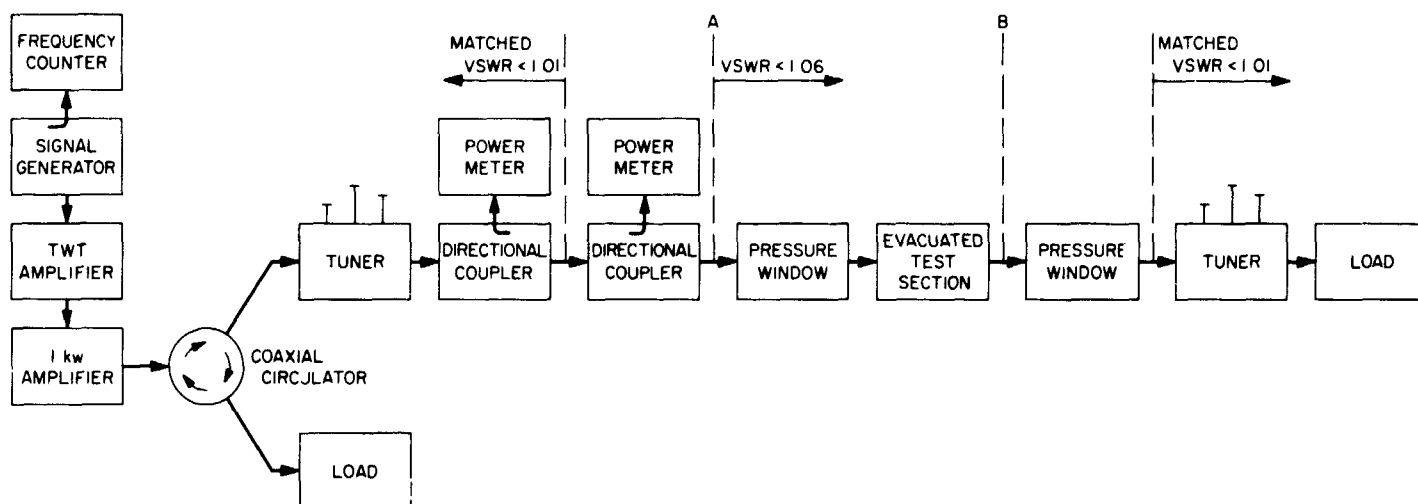


Fig. 9. Schematic of experimental setup

were monitored by Hewlett-Packard 431B power meters connected through appropriate attenuators to the coupling arms of the directional couplers. Coupling figures and attenuation losses were measured within 0.02 db with a Weinschel dual-channel insertion loss test set. Frequency was monitored with a frequency counter. Triple stub tuners were used to attain the matched conditions indicated in Fig. 9.

The vacuum system consisted of a roughing pump and an 8 l/sec vac-ion pump. Low pressures were measured with a built-in meter in the Ultek 60-055 power unit for the vac-ion pump; typical operating pressure levels were 5×10^{-6} mm of Hg. The pressure windows had mechanical seals formed between the Teflon spacers and the copper flanges (Fig. 10). Evacuation of the test section took place through an $\frac{1}{8}$ -in.-diameter hole. The test section was abrasively cleaned immediately before conducting each experiment.

3. Experimental results and discussion

In determining the voltage level in the evacuated test section, the actual power level in the test section, and not merely elsewhere in the test system, must be known. The insertion loss between the forward directional coupler and the test section must, therefore, be measured to permit corrections in the power measurement. The insertion loss measured was less than 0.01 db, making the correction factor almost negligible. Error in the calculation of the voltage level occurs if the assembly of components on the load side of the test section (point B in Fig. 9) has any appreciable VSWR. This measurement was not made because it was physically impossible. However,

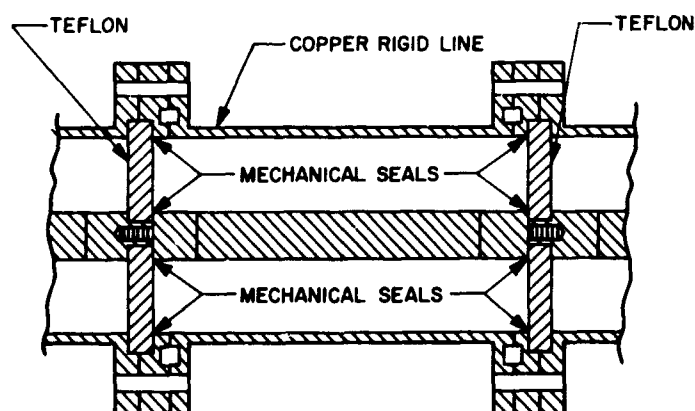


Fig. 10. Evacuated rigid line section

VSWR measurements were made at point A (Fig. 9), and found to be less than 1.06. This implies a VSWR at point B of less than 1.06. As a result, the maximum error of the indicated voltage values would be less than $\pm 3\%$. Fig. 25 of SPS 37-41, Vol. IV, p. 245 is reproduced here as Fig. 11 for reference. As shown, data were obtained for values of fd up to 500 MHz-cm. In the present series of experiments, all values of fd are greater than 958.6. At these higher values of fd , higher order multipacting modes are more likely to occur, and RF voltages considerably greater than 200 v would be necessary. Therefore, with 1 kw RF power (RF voltage is 223.6 v), multipacting was not expected. The summary of data in Table 1 substantiates these predictions.

It is common in the study of microwave breakdown in gases to irradiate the test component with an ionizing source such as Cobalt 60 to obtain more reproducible data.

Table 1. Summary of data

Coaxial rigid line size, in.	Distance between inner and outer conductors (d), cm	Frequency (f), MHz	fd, MHz-cm	Maximum power levels checked, w	Maximum rms voltage levels checked, v	Breakdown
3/8	0.5639	1700	958.6	1000	223.6	No
3/8	0.5639	2000	1127.8	1000	223.6	No
3/8	0.5639	2400	1353.3	875	209.2	No
1 1/8	1.096	1700	1863.2	1000	223.6	No
1 1/8	1.096	2000	2192.0	1000	223.6	No
1 1/8	1.096	2400	2630.4	875	209.2	No

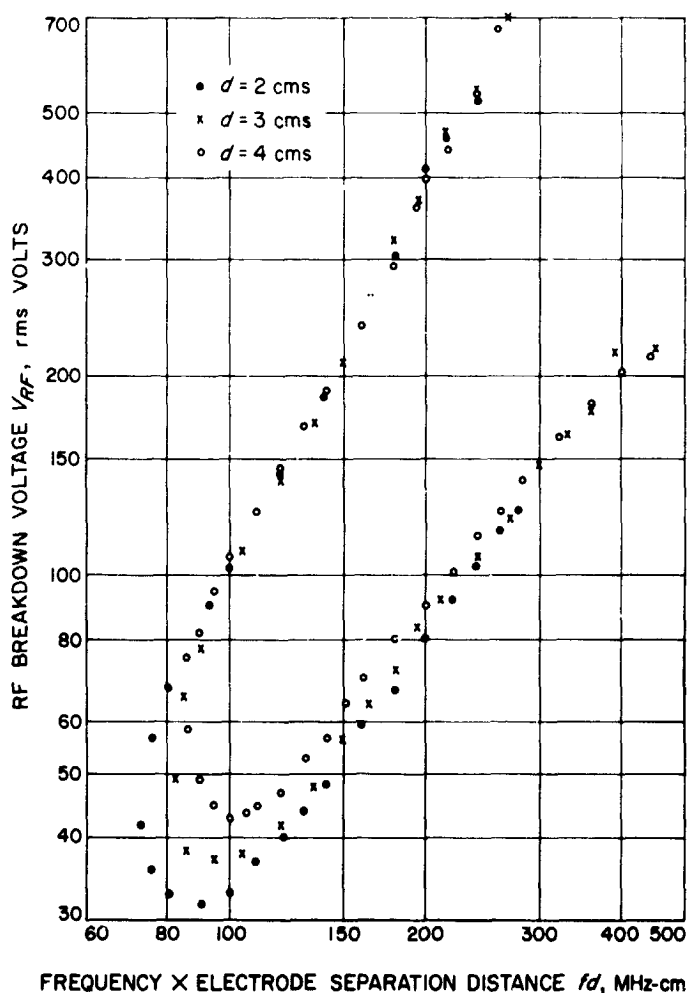


Fig. 11. Multipacting region for coaxial electrodes
 $d = 2, 3, \text{ and } 4 \text{ cms, } b/a = 2.3$

In the experiments described in this article, irradiation was not employed because no data were obtained. It should be noted that irradiation is often unnecessary in CW measurements; this was the case in the multipacting experiments at lower frequencies (SPS 37-41, Vol. IV, pp. 242-246).

When the 1 kw CW RF source on order is delivered, similar experiments using this test setup will be conducted in the frequency range 150 to 1000 MHz. With the 3/8-in. and 1 1/8-in. rigid coaxial line sections, the range of values for fd will be comparable to those in Fig. 11. Thus, an invaluable check of our scaling laws can be made.

D. High Impact Antenna Study: Rectangular Cup Radiator, Part II, K. Woo

1. Introduction

In SPS 37-43, Vol. IV, pp. 386-388, the design theory of a rectangular cup radiator was discussed, and a high impact model of the antenna was described. This article presents the test results of a second high impact model. This model withstood an indirect impact of 10,000 g, and will be tested against direct impacts (refer to SPS 37-40 to 37-42, Vol. IV for other high impact antennas).

2. Antenna Design

The antenna is shown in Fig. 12. It consists of an aluminum rectangular cup, 2.250 in. \times 3.150 in. \times 2.475 in. deep. The cup is excited by a probe (Fig. 13) that is slanted along one of the diagonals of the cup. The probe, a brass rod 3/32 in. in diameter, is an extension of the center conductor of the input coaxial connector located at the rear of the cup. The probe is completely imbedded in Eccofoam to withstand high impacts. The foam was formed by filling the entire cup with Eccofoam FP¹ (foam-in-place liquid resin) and catalyst. Upon curing, the foam gave an all-around rigid support for the probe and the cup walls. The cured foam in this model has a density of about 16 lb/ft³, a relative dielectric constant of about 1.3, a compressive strength of about 700 psi, and an excellent adhesion to the aluminum cup walls.

¹Distributed by Emerson and Cuming, Inc.

(a) FRONT

(b) REAR

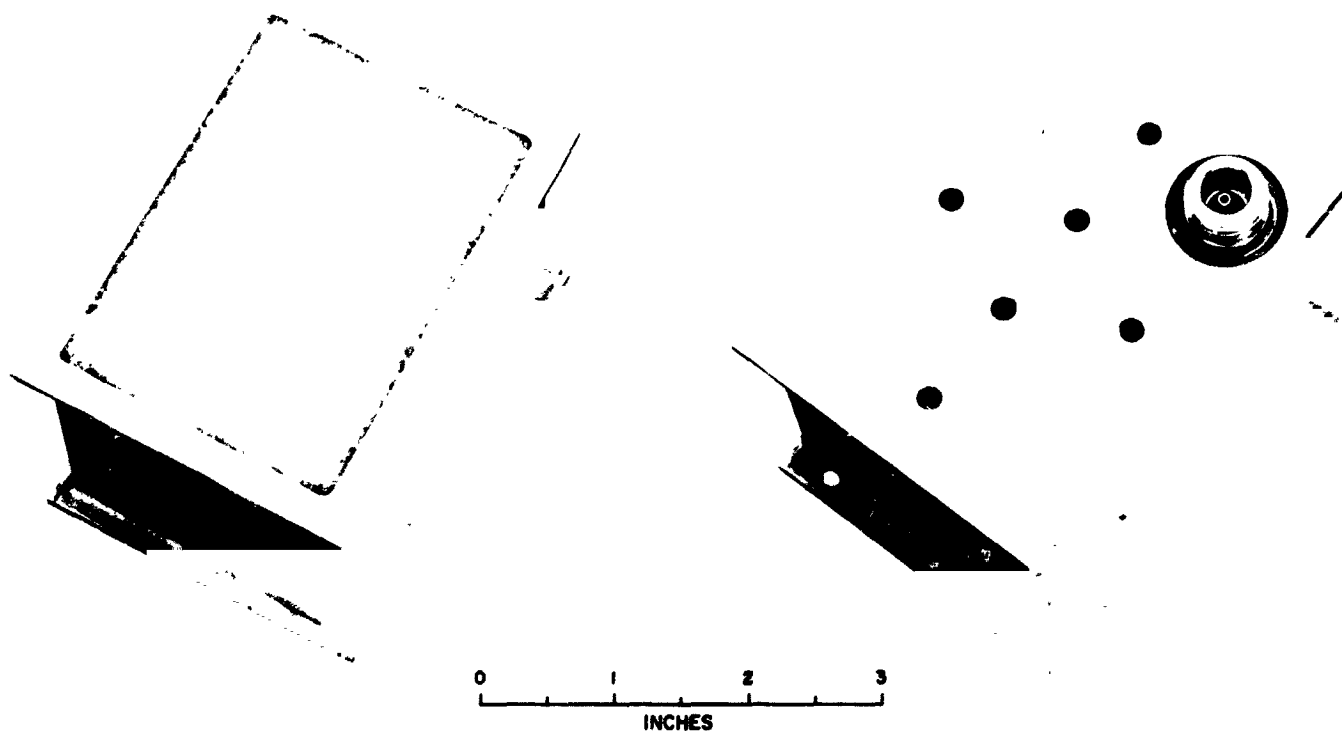


Fig. 12. High impact rectangular cup radiator

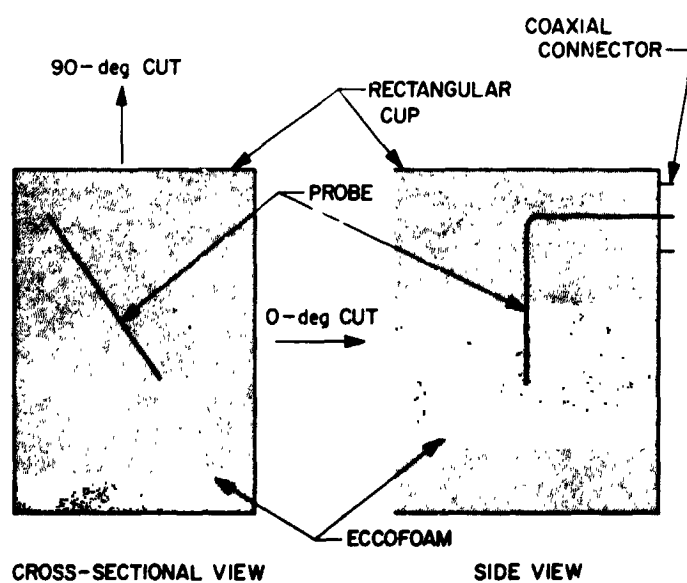


Fig. 13. Schematic of rectangular cup radiator

3. Test Results

Indirect impact test of the antenna at 10,000 g (0.6 msec duration) was performed. The antenna was mounted in a test fixture, and then the fixture was impacted against a target. The cup body was unharmed, and the foam survived the impact without noticeable cracking or separation from the cup walls. There was no appreciable change in the electrical performance of the antenna. Fig. 14 shows the radiation patterns at 2298 MHz along the 90-deg cut (Fig. 13) of the right-hand circularly polarized (RCP) and left-hand circularly polarized (LCP) components taken before and after the impact. The input VSWRs before and after the impact were, respectively, 1.7.

Electrical measurements show that the half-power beamwidth of the antenna varies from a maximum of about 88 deg (along 0-deg cut) to a minimum of about 72 deg (along 90-deg cut).

Further work on the antenna will include:

- (1) Refining the electrical performance.
- (2) Testing survivability against direct impacts.
- (3) Investigating such environmental problems as out-gassing, sterilization, and high power operation.

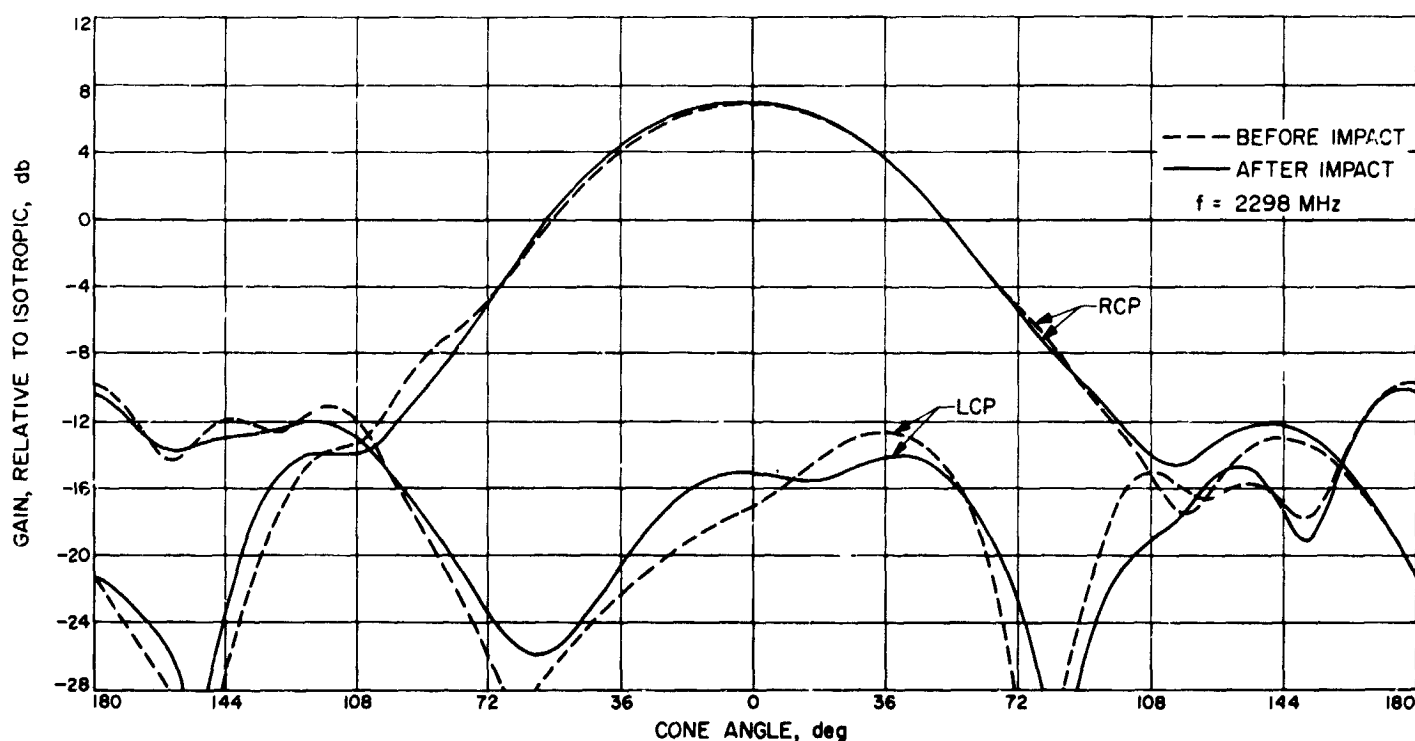


Fig. 14. Radiation patterns before and after impact, 90-deg cut